Journal of Materials Science: Materials in Electronics
https://doi.org/10.1007/s10854-020-02979-7

Magnetic softness, dynamic magnetization, and relaxation behavior of FeSiBC amorphous alloys

Aina He[1,2] · Huiyun Xiao[1] · Yaqiang Dong[1,2] · Anding Wang[1] · Yan Pan[1] · Xiaohong Yang[3] · Jianya Ge[3]

Received: 31 October 2019 / Accepted: 23 January 2020

Abstract
The variation of dynamic coercivity, core loss, permeability (μ'), and relaxation behavior with annealing temperature, frequency as well as magnetic field magnitude (H_m) for the FeSiBC amorphous alloy was systematically studied. It can be found that the dynamic coercivity (H_{cd}) of 6.2 A/m at 1.0 T and 50 Hz is much larger than the static coercivity (H_{cs}) of 1.7 A/m for the optimally annealed $Fe_{78}Si_8B_{13}C_1$ alloy. The increase of H_{cd} with the increases in frequency can be ascribed to the difficulty of domain wall motion and magnetization rotation as frequency elevates. The dynamic magnetization analysis reveals that μ' goes up and attains a peak value as H_m increases to about 25 A/m in the low frequency range, while the μ' does not depend on H_m in the high frequency range ($f > 10$ kHz). In addition, the change of magnetic relaxation time with annealing temperature and filed magnitude is discussed.

1 Introduction

Fe-based amorphous alloys have superior magnetic softness consisting of the large saturation magnetic induction, large permeability, small coercivity, and small core loss due to their small magnetic anisotropies and absence of ordered atomic lattices [1, 2]. These excellent characteristics make the Fe-based amorphous alloys widely used for the transformers, inductors, electric motors, and other electrical devices [3, 4]. Since the ferromagnetic FePC [5] amorphous alloy was first discovered by Duwez et al. in 1967, a large number of Fe-based soft magnetic amorphous alloys have been developed, such as Fe(Co,Ni)SiB [6-8], Fe(Al,Ga)(P,C,B,Si,Ge) [9, 10], FeCoNiCr [11], FeCoSiBNb [12], FeCrMoCB(NiP,Y) [13, 14], FeCo(Ti,Zr)B [15, 16], and Fe(Co)SiBPC [17, 18] systems. Many efforts have been made to improve amorphous forming ability by composition designing and enhance magnetic softness by annealing. In addition, other magnetic materials like magnetic nanoparticles [19] and cobalt–nickel ferrite [20] focused on improving other properties such as photo-catalytic, besides the magnetic softness. However, there are only few studies on dynamic magnetic behavior of Fe-based amorphous alloys, especially the frequency of more than 1 kHz.

Nevertheless, dynamic magnetization consideration is one of the most key influence factors for electronics design. Because the Fe-based amorphous alloys as core materials are often subjected to the AC excitation magnetic field, dynamic coercivity (H_{cd}), core loss, and permeability change with frequencies and field magnitudes [21, 22]. The knowledge on these dynamic responses is conducive to the designers to select the appropriate materials and operating conditions in the practical applications. Moreover, the dynamic magnetic properties are related to dynamic responses of the magnetic domain walls movement and magnetization rotation [23, 24]. These responses also cause the dynamic magnetic relaxation, but the factors affecting the relaxation are still not thorough.

The purpose of this paper is therefore to provide a comprehensive view of annealing temperature, frequencies and exciting field magnitudes dependence of dynamic coercivity, core loss, permeability, as well as magnetic relaxation

✉ Yaqiang Dong
dongyq@nimte.ac.cn

✉ Anding Wang
anding.w@hotmail.com

✉ Jianya Ge
gejy1965@aliyun.com

[1] CAS Key Laboratory of Magnetic Materials and Devices, Zhejiang Province Key Laboratory of Magnetic Materials and Application Technology, Ningbo Institute of Materials Technology and Engineering, Chinese Academy of Sciences, Ningbo 315201, Zhejiang, China

[2] University of Chinese Academy of Sciences, Beijing 100049, China

[3] Jinhua Polytechnic, Jinhua 321007, Zhejiang, China

Published online: 03 February 2020

for the FeSiBC amorphous alloy. The correlations among the dynamic magnetic behavior, frequencies, field magnitude together with annealing temperatures of the amorphous alloys are discussed. Furthermore, the magnetic relaxation time versus annealing temperature and field magnitudes was calculated by means of Havriliak–Negami (H–N) relaxation equation [23, 25].

2 Experimental procedure

The synthesis of amorphous alloy ribbons is divided into three main process: master alloys melting, rapid quenching, and annealing, as shown in Fig. 1. First of all, quaternary master alloys with nominal atomic compositions of $Fe_{78}Si_{9-x}B_{13}C_x$ ($x = 1$, 3, and 5) were prepared by a medium frequency induction furnace with the mixtures of pure Fe (99.99 wt%), Si (99.999 wt%), B (99.5 wt%), and Fe–C prealloy (3.6 wt% C) under an Ar atmosphere. Secondly, ribbons with width of about 1.2 mm and thickness of 21 µm were subsequently obtained by a rapid quenching method. The as-quenched (AQ) ribbons were then cut into length of 7 cm for subsequent annealing and magnetic properties measurements. Finally, these ribbons were sealed in a quartz tube and inserted into a preheated furnace to be annealed. Annealing was carried out at 340–440 °C for 10 min in vacuum. The AQ and annealed ribbons were confirmed to be full amorphous structure by an X-ray diffraction (XRD, Bruker D8 Advance) with Cu Kα radiation.

Static coercivity (H_{cs}) was measured by a DC *B-H* loop tracer (Riken BHS-40) under a field of 800 A/m. Saturation magnetization (M_s) was determined with a vibrating sample magnetometer (VSM, Lakeshore 7410) under a field of 800 kA/m. Dynamic coercivity (H_{cd}) was performed by an AC *B–H* loop tracer (Riken ACBH-100K) under frequencies of 50 Hz and 1 kHz. Real part of complex permeability (μ') at a frequency range from 500 Hz to 10 MHz was measured using an impedance analyzer (Agilent 4294) with varying amplitude of AC magnetic field (H_m) from 1 to 55 A/m. Scanning electron microscope (SEM, FEI Quanta FEG 250) was used to observe the surface morphology. The presence of Fe, Si, and C elements was analyzed by EDS spectrum. High-resolution transmission electron microscopy (HR-TEM) and selected area electron diffraction (SAED) images conducted on Talos F200x were used to characterize the microstructure of the AQ and annealed samples. The specimens for TEM observations were prepared by ion milling (Gatan 691). Magnetic domain structures were observed on the air surface of the ribbon samples by a magneto-optical Kerr microscopy (4-873K/950MT, Germany). All the measurements were carried out at room temperature.

3 Results and discussion

3.1 Magnetic softness and magnetic domains

All the $Fe_{78}Si_{9-x}B_{13}C_x$ ($x = 1$, 3, and 5) alloy ribbons exhibit good surface quality and bending ductility spun at a wheel speed of 40 m/s. The SEM images and EDS spectra of the three as-quenched (AQ) alloy ribbons are displayed in Fig. 2. All the three ribbons show a disorder and uniform structure without crystallization grains (Fig. 2a1–c1). As shown in Fig. 2a2–c2, the presence of Fe, Si, and C elements was observed in EDS spectra in all the three alloys. However, the B element is unable to be detected by the EDS and is not presented in Fig. 2. The three alloy samples for soft magnetic properties measurements were isothermal annealed for 10 min, and the results are displayed in Fig. 3. It can be seen from Fig. 3a–c that the lowest values of static coercivity (H_{cs}) and core loss at 1 T and 1 kHz ($P_{1.0/1k}$), as well as the highest value of

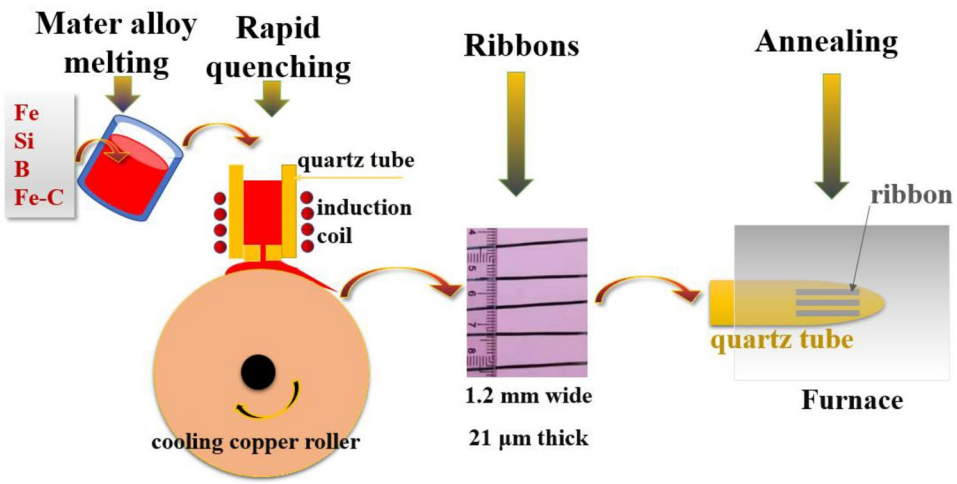

Fig. 1 Schematic diagram of the synthesis process of the alloy ribbons

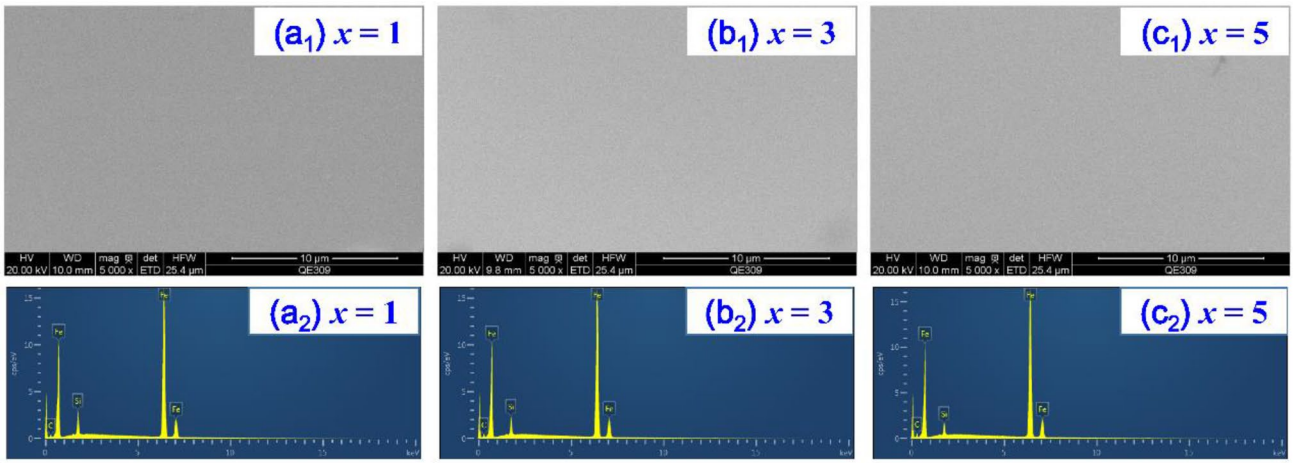

Fig. 2 SEM images and EDS spectra of the as-quenched (AQ) $Fe_{78}Si_{9-x}B_{13}C_x$ ($x = 1$, 3, and 5) alloy ribbons

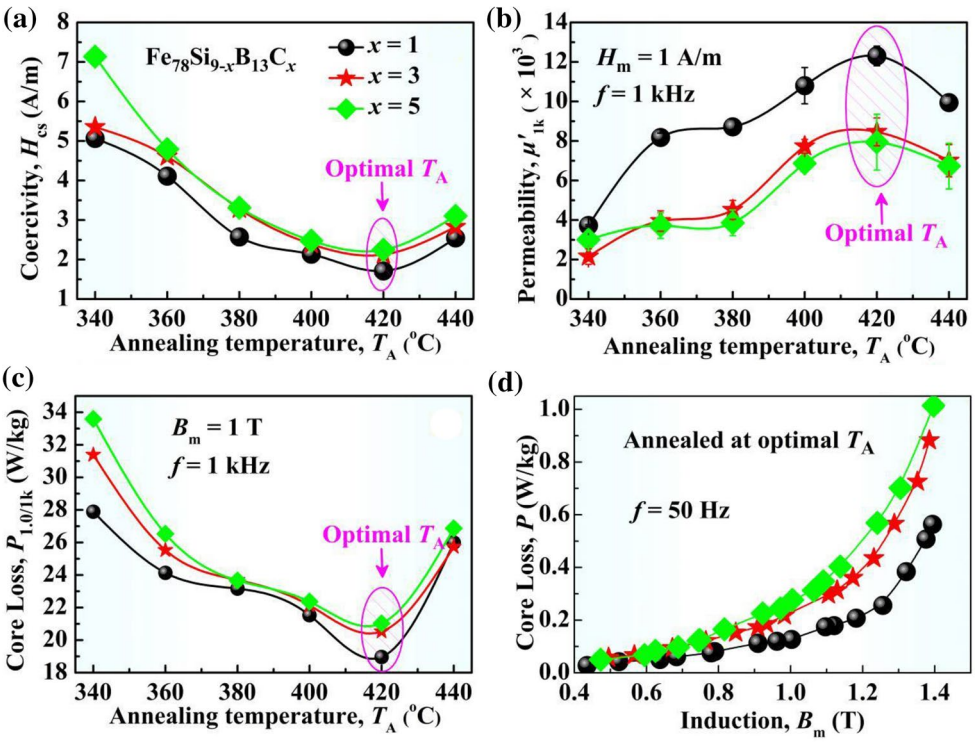

Fig. 3 Static coercivity (H_{cs}, **a**), permeability at 1 kHz (μ'_{1k}, **b**), and core loss at 1 T and 1 kHz ($P_{1.0/1k}$, **c**) as a function of annealing temperature for the $Fe_{78}Si_{9-x}B_{13}C_x$ ($x = 1$, 3, and 5) alloys. **d** Core loss as a function of induction for the optimal annealed alloys at a frequency of 50 Hz

permeability at 1 kHz (μ'_{1k}), were obtained at the annealing temperature (T_A) of 420 °C (henceforth referred to optimal T_A) for the three alloys. The core loss measured at 50 Hz for the three alloys annealed at optimal T_A shows a non-linear increase with the ascending B_m (Fig. 3d). In addition, the magnetic softness of the FeSiBC alloy with $x = 1$ is much better than that of the alloys with $x = 3$ and 5. Since the solubility of C in Fe is very small, the excessive addition of the C content may cause a compositional segregation in the FeSiBC alloys. This segregation leads to form a non-uniform structure, and thus it deteriorates soft magnetic performances of the FeSiBC alloys with high C content.

Figure 4a presents the histograms of the H_{cs}, $P_{1.0/50}$, and μ'_{1k} for the as-quenched (AQ) and annealed $Fe_{78}Si_8B_{13}C_1$ amorphous alloy. It can be found that the H_{cs} is inversely proportional to μ'_{1k} for the $Fe_{78}Si_8B_{13}C_1$ alloy, which is common in the iron-based amorphous and nanocrystalline alloys [18, 26, 27]. On the other hand, the M_s for samples with T_A of 420 °C is larger than that for samples with T_A of 360 and 440 °C, as shown in Fig. 4b. The variation trend of M_s with T_A is opposite to that of H_c with T_A for the $Fe_{78}Si_8B_{13}C_1$

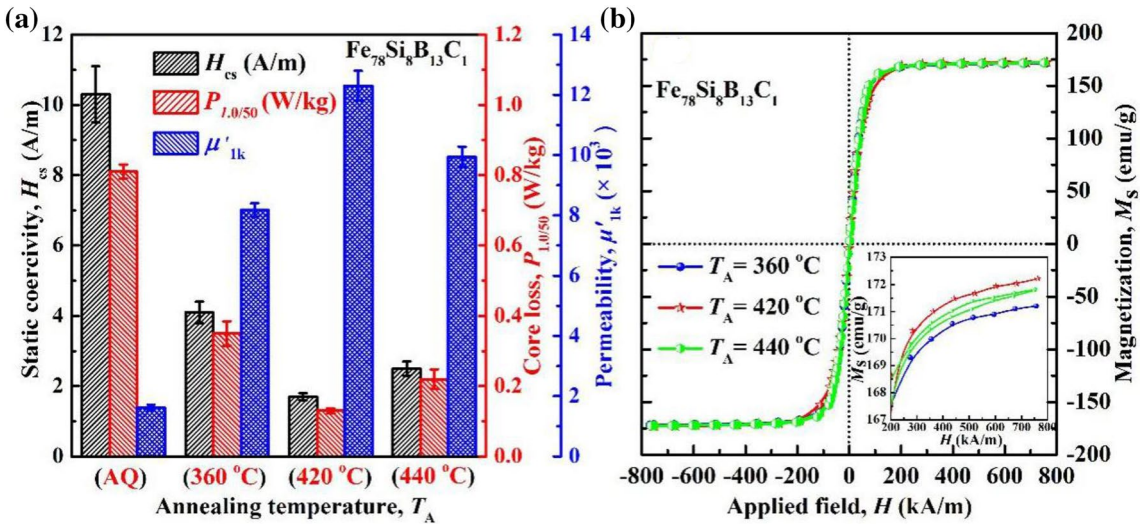

Fig. 4 **a** Magnetic softness histograms for the as-quenched and annealed $Fe_{78}Si_8B_{13}C_1$ amorphous alloys; black, red, and blue columns denote the H_{cs}, $P_{1.0/50}$, and μ'_{1k}, respectively. **b** Hysteresis loops for the $Fe_{78}Si_8B_{13}C_1$ alloy annealed at different T_A. Inset of **b** shows the partial enlarged graph of hysteresis loops. Here, $P_{1.0/50}$ is core loss at 50 Hz under the induction of 1.0 T (Color figure online)

alloy ribbon, which is consistent with other soft magnetic alloys [11, 28]. In order to figure out the origin of changes of magnetic softness with T_A, microstructure and magnetic domains of the AQ and annealed $Fe_{78}Si_8B_{13}C_1$ alloy ribbons were observed with a TEM and magnetic-optical Kerr Microscopy. The HR-TEM images and SAED patterns in Fig. 5 exemplify the evolution of microstructure under AQ state and after annealing at 420 °C and 440 °C for 10 min. The AQ ribbon shows uniform microstructure in the HR-TEM image (Fig. 5a) and diffuse rings in the SAED pattern (inset of Fig. 5a), indicating the presence of the fully amorphous structure. Annealing at 420 °C generates homogeneity of chemical dispersion that is visible as less contrast variation in the HR-TEM image (Fig. 5b). Annealing promotes release of stress and decrease of free volume, and thus it makes the microstructure more uniform. This more uniform microstructure causes better soft magnetic properties, which is consistent with FeSiBPC [29] and Co-based amorphous alloys [28]. After annealing at 440 °C, a typical amorphous structure with several clusters is displayed in the HR-TEM image (Fig. 5c), which is also proved by the SAED image (inset of Fig. 5c). Here, the size of clusters is of ~ 5 nm in diameter. As documented, grain size is closely related to the structure and magnetic properties of nanocrystalline [30] and polycrystalline films [31]. The magnetic domain walls around grain boundaries in the polycrystalline films affect their magnetic properties [31]. Thus, these clusters act as pinning sites of domain walls and hider the magnetization rotation, resulting in the deterioration of the magnetic characteristics. Figure 6 shows the magnetic domain structures for $Fe_{78}Si_8B_{13}C_1$ amorphous alloy with (a) the as-quenched state (AQ), and annealed at (b) 360 °C, (c) 420 °C, and (d)

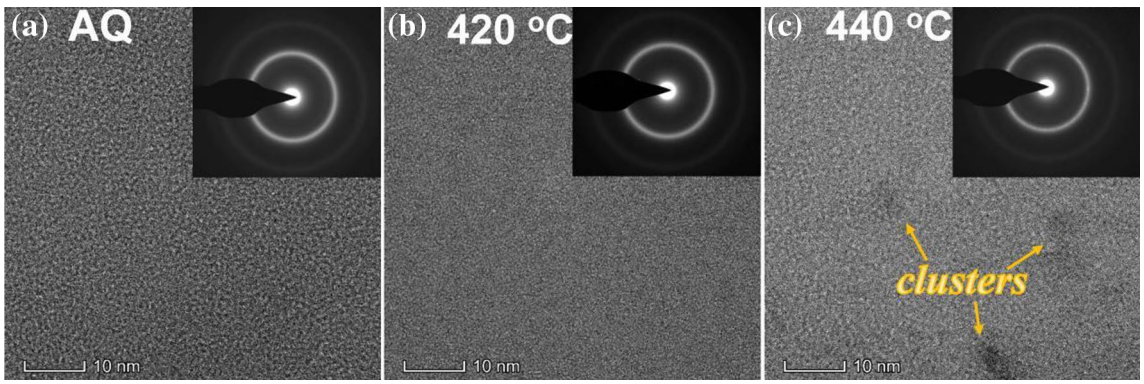

Fig. 5 TEM images for $Fe_{78}Si_8B_{13}C_1$ amorphous alloy with **a** the as-quenched state (AQ), and annealed at **b** 420 °C and **c** 440 °C for 10 min, respectively. The corresponding SAED patterns are displayed in the inset

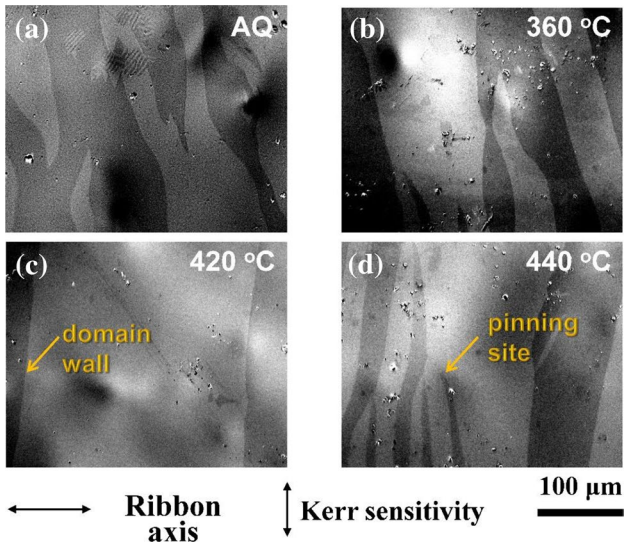

Fig. 6 Magnetic domain structures for $Fe_{78}Si_8B_{13}C_1$ amorphous alloy with **a** the as-quenched state (AQ), and annealed at **b** 360 °C, **c** 420 °C, and **d** 440 °C for 10 min, respectively

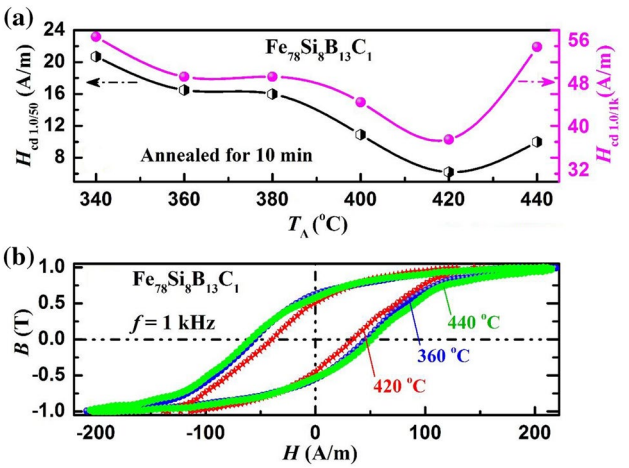

Fig. 7 **a** The dynamic coercivity ($H_{cd1.0/50}$ and $H_{cd1.0/1k}$) as a function of T_A for the $Fe_{78}Si_8B_{13}C_1$ amorphous alloy annealed for 10 min. **b** Dynamic hysteresis loops at a frequency of f = 1 kHz for samples annealed at 360, 420, and 440 °C, respectively. Here, $H_{c1.0/05}$ is the dynamic coercivity at 50 Hz under the induction of 1.0 T, and $H_{c1.0/1k}$ is the dynamic coercivity at 1 kHz under the induction of 1.0 T

440 °C for 10 min, respectively. It can be found that the AQ sample has disorder and irregular domain patterns (Fig. 6a), ascribing to the strong internal stress and structural inhomogeneity coming from the rapid quenching process [10]. With rising of T_A, the domain walls straighten and the number of walls decreases due to the stress release [32], resulting in the improvement of the magnetic softness. However, when the T_A rises up to 440 °C, the emergence of new pinning sites may result from the formation of clusters, which makes the domain structure change from wide regular domains (Fig. 6c) to small irregular domains (Fig. 6d), resulting in the deterioration of the magnetic softness. Thus, it can be concluded that the variation of domain structure with T_A is well consistent with change of magnetic softness with T_A [33, 34].

3.2 Dynamic magnetization behavior

Since soft magnetic amorphous materials always used in AC magnetic field with various field amplitudes and frequencies, it is essential to study the dynamic magnetic properties of amorphous alloys. Figure 7a displays the dynamic coercivity at 1.0 T and 50 Hz ($H_{cd1.0/50}$), as well as at 1.0 T and 1 kHz ($H_{cd1.0/1k}$) as a function of T_A for the $Fe_{78}Si_8B_{13}C_1$ amorphous alloy annealed for 10 min. The $H_{cd1.0/50}$ and $H_{cd1.0/1k}$ have the similar trend with the elevation of T_A, and the lowest values are 6.2 and 37.8 A/m at the optimal T_A of 420 °C, respectively. Figure 7b illustrates the dynamic hysteresis loops at 1 kHz for the annealed samples. It can be observed that the applied magnetic field (H) at the optimal T_A of 420 °C (144 A/m) is smaller than that at 360 °C (185 A/m) and 440 °C (215 A/m), when the magnetic induction (B) achieves 1.0 T. Thus, we can conclude that the dynamic coercivity (H_{cd}) is much larger than the static coercivity (H_{cs}) in the FeSiBC amorphous alloy, and their relations can be expressed as follows [35]:

$$H_{cd} = H_{cs} + A\,(fH)^{1/n}, \tag{1}$$

where A is the proportionality constant, H is the applied magnetic field, and n is the coefficient depending on geometry and hysteresis loop of the alloys. The f dependence of the H_{cd} can be ascribed to the variation of dynamic magnetization process activity at increasing f. With increasing f, the magnetic domain is refined and the number of domain walls increases [24], which leads to the difficulty of domain wall motion and magnetization rotation, resulting in the increase of dynamic coercivity (H_{cd}).

For evaluating the influence of T_A on dynamic magnetization behavior for the $Fe_{78}Si_8B_{13}C_1$ amorphous ribbons, permeability (μ') spectrum has been measured at the frequency (f) range from 500 to 1×10^7 Hz and the amplitude of AC magnetic field (H_m) from 1 to 55 A/m, and the results are shown in Fig. 8. The curves measured at all H_m show that μ' falls down with f going up, because the magnetization process becomes unable to follow the AC magnetic field with the increase in f, resulting in the increment of the eddy current loss and appearance of magnetic relaxation [11, 23]. On the other hand, the frequency stability of μ' becomes more stable with the increases of H_m. Two-dimensional color map is used to more clearly observe the change of μ' for the AQ and annealed samples with f and H_m, as shown

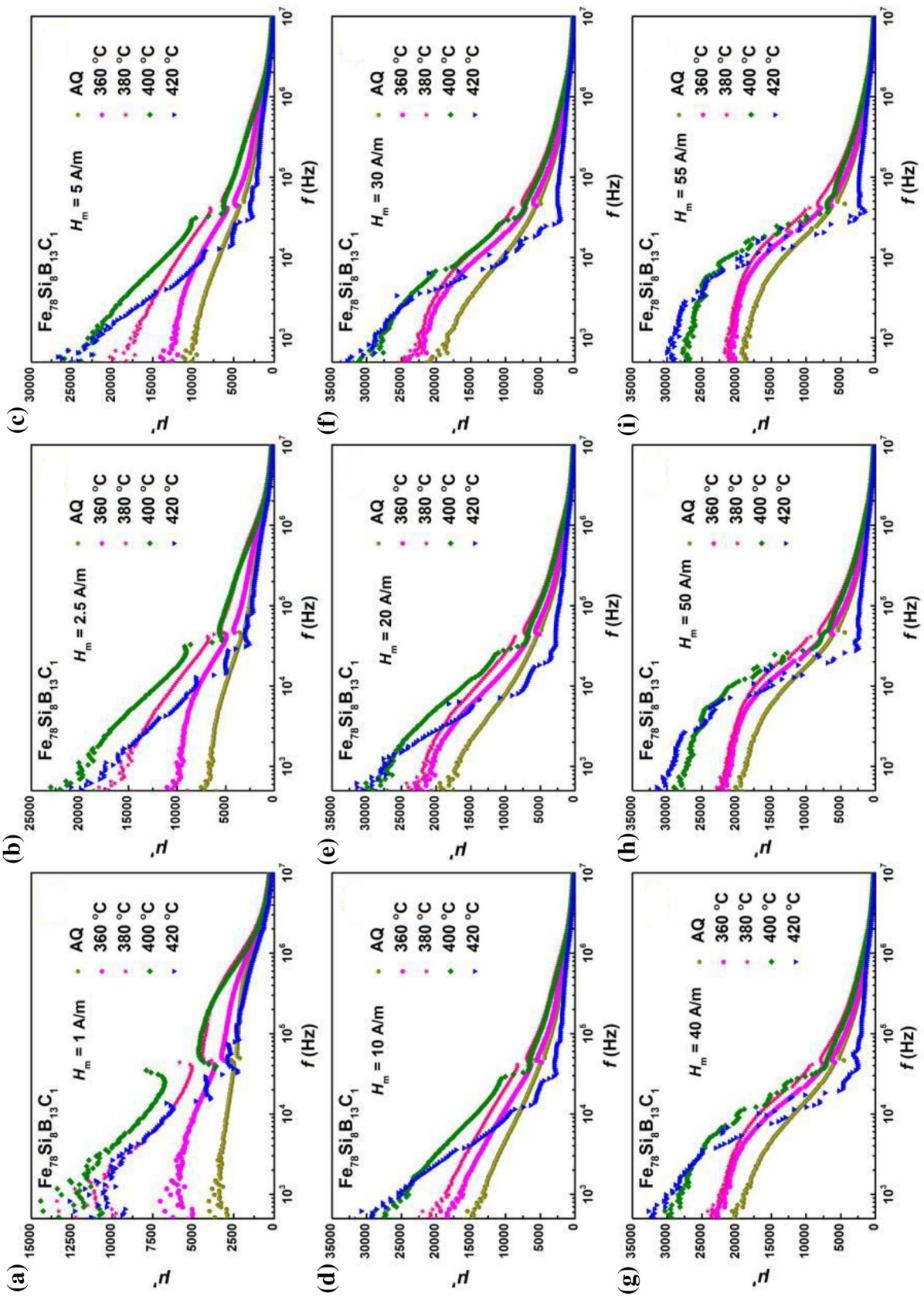

Fig. 8 Permeability (μ') as a function of magnetization frequency (f) for the as-quenched (AQ) and annealed $Fe_{78}Si_8B_{13}C_1$ amorphous alloy measured at various field magnitudes (H_m): **a** 1 A/m, **b** 2.5 A/m, **c** 5 A/m, **d** 10 A/m, **e** 20 A/m, **f** 30 A/m, **g** 40 A/m, **h** 50 A/m, and **i** 55 A/m

in Fig. 9. The value of μ' increases with the rises of T_A for the $Fe_{78}Si_8B_{13}C_1$ samples measured at all H_m and the frequency less than 10 kHz. According to the studies of Dobák et al., the μ' is closely related to domain wall movement and magnetization rotation [36]. In addition, the rotation of magnetization and movement of domain wall are correlation to the magnetic anisotropy, internal stress, spinning effect, as well as structural inhomogeneity [10]. Therefore, the μ' rises with elevation of the T_A for $Fe_{78}Si_8B_{13}C_1$ alloy ribbon are ascribed to the fact that the motion of domain wall and rotation of magnetization become easier due to strain releasing, microstructure homogenizing, and pinning effect reducing. Furthermore, it can be found that the μ' goes up and attains a peak value as H_m increases to a certain amplitude of about 25 A/m in the low-frequency region. However, the μ' in the high-frequency region ($f > 10$ kHz) does not depend on H_m. This indicates that the magnetic relaxation process in the high-frequency region is different from that in the low-frequency region [37].

3.3 Magnetic relaxation

To further analyze the T_A dependence of dynamic magnetization processes and magnetic relaxation for the as-quenched and annealed $Fe_{78}Si_8B_{13}C_1$ amorphous alloy ribbons, the experimental μ' is theoretically fitted by using a Havriliak–Negami (H–N) relaxation model. This H–N model is expressed as the following equation [23, 25, 38]:

$$\mu'(\omega) = \mu'_{\infty} + \frac{(\mu'_s - \mu'_{\infty})\cos(\beta\phi)}{(1 + 2(\omega\tau_r)^{1-\alpha} + (\omega\tau_r)^{2(1-\alpha)})^{\frac{\beta}{2}}} \quad (2)$$

with

$$\phi = \arctan\left[\frac{(\omega\tau_r)^{1-\alpha}\sin(\pi(1-\alpha)/2)}{1 + (\omega\tau_r)^{1-\alpha}\cos(\pi(1-\alpha)/2)}\right] \quad (3)$$

and

$$\mu'_s = \lim_{\omega \to 0}\mu' \quad (4)$$

and

$$\mu'_{\infty} = \lim_{\omega \to \infty}\mu', \quad (5)$$

where $\omega = 2\pi f$, τ_r is the chief relaxation time, and the exponents α ($0 \le \alpha < 1$) and β ($0 < \beta \le 1$) are, respectively, connected with the width and asymmetry of the relaxation time distribution [23, 39, 40].

To investigate the relaxation dispersion observed in the permeability of the AQ and annealed $Fe_{78}Si_8B_{13}C_1$ amorphous alloy, we plot μ' as function of f at field magnitude of 5 A/m in Fig. 10 as a representative. It can be seen from Fig. 10 that the theoretical fitting curves agree well with the experimental μ' curves, and the goodness of fit for the AQ and annealed $Fe_{78}Si_8B_{13}C_1$ amorphous alloy at all measurement filed magnitudes is above 0.996.

In this fitting, the exponents α and β are related to the distribution of relaxation behavior, were obtained through

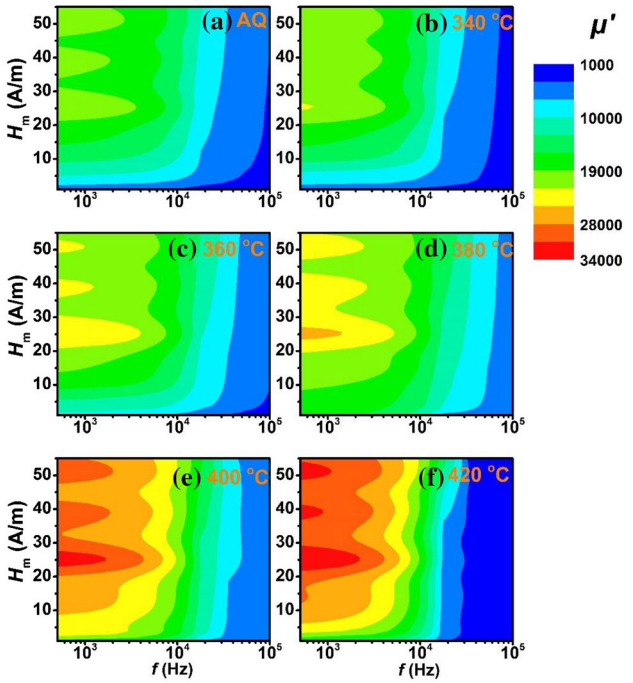

Fig. 9 Color map of permeability (μ') as a function of magnetization frequency (f) and amplitude of AC magnetic field (H_m) for the $Fe_{78}Si_8B_{13}C_1$ amorphous ribbons with **a** the as-quenched (AQ) state, and T_A of **b** 340 °C, **c** 360 °C, **d** 380 °C, **e** 400 °C, **f** 420 °C (Color figure online)

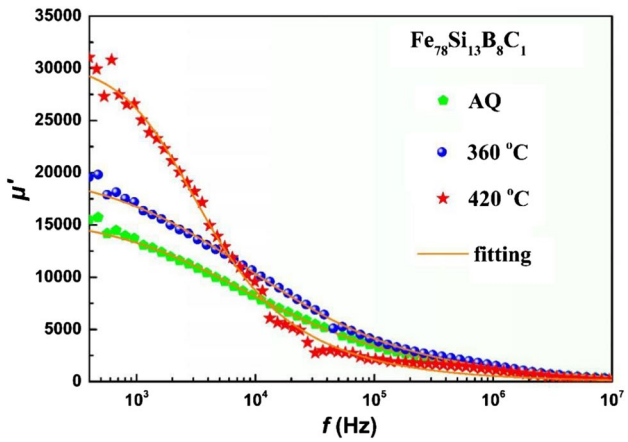

Fig. 10 Permeability (μ') as a function of frequency (f) for the as-quenched (AQ) and annealed $Fe_{78}Si_8B_{13}C_1$ amorphous alloys measured at 5 A/m. Theoretical fits μ' using H–N relaxation model are solid curves

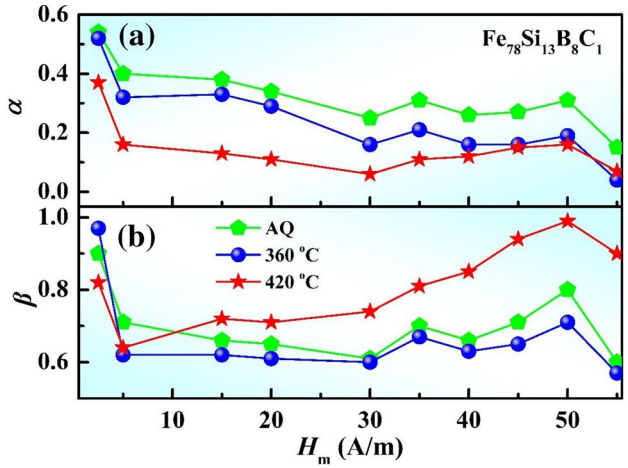

Fig. 11 Field magnitude (H_m) evolution of exponents **a** α and **b** β of H–N relaxation model obtained from the best fitting of experimental μ' for the as-quenched (AQ) and annealed $Fe_{78}Si_8B_{13}C_1$ amorphous alloys

the fitting of H–N model equation under different H_m, and the results are provided in Fig. 11. The exponent α of the 420 °C annealed sample is lower than that of the AQ and 360 °C annealed samples at H_m from 1 to 50 A/m. However, the exponent β of the 420 °C annealed sample is higher than that of AQ and 360 °C annealed samples at H_m from 15 to 55 A/m. Table 1 lists the exponents α and β, chief relaxation time τ_r for the AQ and annealed $Fe_{78}Si_8B_{13}C_1$ amorphous alloys. It can be found that the τ_r of the 420 °C annealed sample is lower than that of the AQ and 360 °C annealed samples measured at most H_m. Since distribution of relaxation times is connected to the motion of domain walls [40], this phenomenon may be ascribed to more losses caused by damping and pinning effect of movement of domain walls for the sample annealed at 420 °C, compared to that for the AQ and 360 °C annealed samples. These results indicate that the annealing treatment rises the change in the width of loss peak and relaxation time, which can explain the variation of H_{cd} and μ' with increasing T_A.

4 Conclusions

The magnetic softness, magnetic domains, dynamic magnetization process, and magnetic relaxation of the as-quenched and annealed FeSiBC amorphous alloys are analyzed. It has been found that the static coercivity and core loss in the $Fe_{78}Si_8B_{13}C_1$ amorphous alloy reach much lower values than that in the $Fe_{78}Si_6B_{13}C_3$ and Fe78Si4B13C5 alloys. The optimal magnetic softness, such as the lowest coercivity, the lowest core loss, the highest permeability, obtained in the $Fe_{78}Si_8B_{13}C_1$ alloy annealed at 420 °C can be ascribed to the releasing of stress and presence of wide as well as straight magnetic domains. The dynamic magnetization analysis reveals that μ' increases with the rise of T_A for the $Fe_{78}Si_8B_{13}C_1$ samples measured at all H_m and the frequency less than 10 kHz. Moreover, μ' goes up and attains a peak value as H_m increases to a certain amplitude of about 25 A/m in the low frequency range. However, the μ' in the high frequency range ($f > 10$ kHz) does not depend on H_m. Furthermore, from best fitting of μ' versus f using H–N relaxation equation, it can be found that annealing treatment and field magnitude impact on the magnetic relaxation time, resulting in variation of H_{cd} and μ' with increasing T_A.

Table 1 The exponents α and β, as well as chief relaxation time τ_r obtained from best fit of the experimental μ' and H–N model under the different field magnitude (H_m) for the as-quenched (AQ) $Fe_{78}Si_8B_{13}C_1$ amorphous alloy, and the alloy annealed at T_A of 360 °C and 420 °C

H_m (A/m)	AQ			$T_A = 360$ °C			$T_A = 420$ °C		
	α	β	τ_r (μs)	α	β	τ_r (μs)	α	β	τ_r (μs)
2.5	0.54	0.90	8.7	0.52	0.97	2.5	0.37	0.82	69.4
5	0.40	0.71	17.4	0.32	0.62	15.9	0.16	0.64	83.5
10	0.41	0.74	31.1	0.46	0.90	20.6	0.12	0.66	75.8
15	0.38	0.66	56.1	0.33	0.62	78.6	0.13	0.72	57.9
20	0.34	0.65	55.1	0.29	0.61	72.3	0.11	0.71	63.5
25	0.40	0.77	44.9	0.33	0.79	23.2	0.18	0.82	47.8
30	0.25	0.61	38.0	0.16	0.6	23.1	0.06	0.74	38.7
35	0.31	0.70	29.7	0.21	0.67	19.1	0.11	0.81	31.3
40	0.26	0.66	26.4	0.16	0.63	17.9	0.12	0.85	26.3
45	0.27	0.71	20.7	0.16	0.65	15.4	0.15	0.94	20.0
50	0.31	0.80	16.1	0.19	0.71	13.0	0.16	0.99	16.6
55	0.15	0.60	17.3	0.04	0.57	13.4	0.07	0.90	14.2

Acknowledgements This work was supported by the National Key Research and Development Program of China (Grant No. 2016YFB0300500), the National Natural Science Foundation of China (Grant Nos. 51801224, 51771083, 51701136), the Zhejiang Provincial Natural Science Foundation (Grant No. LQ18E010006), the Ningbo Municipal Natural Science Foundation (Grant No. 2018A610172), and Science and Technology Service Network Initiative (Grant No. KFJ-STS-SCYD-220).

References

1. G. Herzer, Modern soft magnets: amorphous and nanocrystalline materials. Acta Mater. **61**, 718–734 (2013)
2. R. Hasegawa, Advances in amorphous and nanocrystalline materials. J. Magn. Magn. Mater. **324**, 3555–3557 (2012)
3. J.M. Silveyra, E. Ferrara, D.L. Huber, T.C. Monson, Soft magnetic materials for a sustainable and electrified world. Science. **362**, eaao0195 (2018)
4. O. Gutfleisch, M.A. Willard, E. Brück, C.H. Chen, S.G. Sankar, J.P. Liu, Magnetic materials and devices for the 21st century: stronger, lighter, and more energy efficient. Adv. Mater. **23**, 821–842 (2011)
5. P. Duwez, S.C.H. Lin, Amorphous ferromagnetic phase in iron-carbon-phosphorus alloys. J. Appl. Phys. **38**, 4096–4097 (1967)
6. G. Kumar, M. Ohnuma, T. Furubayashi, T. Ohkubo, K. Hono, Thermal embrittlement of Fe-based amorphous ribbons. J. Non-Cryst. Solids **354**, 882–888 (2008)
7. G.H. Hayes, W.A. Hines, D.P. Yang, J.I. Budnick, Low field magnetic anisotropy in Metglas 2605 CO ribbons. J. Appl. Phys. **57**, 3511 (1985)
8. K. Inomata, T. Sawa, M. Hasegawa, Magnetostriction and magnetic core loss at high-frequency in amorphous Fe-based alloys. J. Appl. Phys. **57**, 3572–3574 (1985)
9. A. Makino, A. Inoue, T. Mizushima, Soft magnetic properties Fe-based Bulk amorphous alloys. Mater. Trans. JIM **41**, 1471–1477 (2000)
10. T. Bitoh, A. Makino, A. Inoue, Origin of low coercivity of Fe-(Al, Ga)-(P, C, B, Si, Ge) bulk glassy alloys. Mater. Trans. JIM **44**, 2020–2024 (2003)
11. R.H. Yu, High-temperature AC magnetic properties of FeCo-based soft magnets. J. Magn. Magn. Mater. **284**, 140–144 (2004)
12. J. Fornell, S. González, E. Rossinyol, S. Suriñach, M.D. Baró, D.V. Louzguine-Luzgin, J.H. Perepezko, J. Sort, A. Inoue, Enhanced mechanical properties due to structural changes induced by devitrification in Fe–Co–B–Si–Nb bulk metallic glass. Acta Mater. **58**, 6256–6266 (2010)
13. B. Bochtler, I. Gallino, R. Busch, Thermo-physical characterization of the $Fe_{67}Mo_6Ni_{3.5}Cr_{3.5}P_{12}C_{5.5}B_{2.5}$ bulk metallic glass forming alloy. Acta Mater. **118**, 129–139 (2016)
14. D.V. Louzguine-Luzgin, A.I. Bazlov, S.V. Ketov, A.L. Greer, A. Inoue, Crystal growth limitation as a critical factor for formation of Fe-based bulk metallic glasses. Acta Mater. **82**, 396–402 (2015)
15. S.N. Kane, M. Coisson, P. Tiberto, F. Vinai, F. Mazaleyrat, On the influence of Joule heating induced nanocrystallization on structural and magnetic properties of $Co_{64}Fe_{21}B_{15}$ alloy. Curr. Appl. Phys. **11**, 981–985 (2011)
16. B. Han, Y.K. Kim, H. Choi-Yim, Effect of compositional variation on the soft magnetic properties of $Fe_{(87-x-y)}Co_xTi_7Zr_6B_y$ amorphous ribbons. Curr. Appl. Phys. **14**, 685–687 (2014)
17. C.L. Zhao, A.D. Wang, S.Q. Yue, T. Liu, A.N. He, C.T. Chang, X.M. Wang, C.-T. Liu, Significant improvement of soft magnetic properties for Fe(Co)BPSiC amorphous alloys by magnetic field annealing. J. Alloys Compd. **742**, 220–225 (2018)
18. W.J. Yuan, S.J. Pang, F.J. Liu, T. Zhang, Frequency and magnetic field dependences of coercivity and core loss in Fe–Mo–Si–P–C–B amorphous alloys. J. Alloys Compd. **504**, S142–S145 (2010)
19. M.A. Marsooli, M. Fasihi-Ramandi, K. Adib, S. Pourmasoud, F. Ahmadi, M.R. Ganjali, A. Sobhani Nasab, M.R. Nasrabadi, M.E. Plonska-Brzezinska, Preparation and characterization of magnetic $Fe_3O_4/CdWO_4$ and $Fe_3O_4/CdWO_4/PrVO_4$ nanoparticles and investigation of their photocatalytic and anticancer properties on PANC1 cells. Materials (Basel) (2019). https://doi.org/10.3390/ma12193274
20. S.M. Peymani-Motlagh, A. Sobhani-Nasab, M. Rostami, H. Sobati, M. Eghbali-Arani, M. Fasihi-Ramandi, M.R. Ganjali, M. Rahimi-Nasrabadi, Assessing the magnetic, cytotoxic and photocatalytic influence of incorporating Yb3+ or Pr3+ ions in cobalt–nickel ferrite. J. Mater. Sci. Mater. Electron. **30**, 6902–6909 (2019)
21. F. Fiorillo, DC and AC magnetization processes in soft magnetic materials. J. Magn. Magn. Mater. **242–245**, 77–83 (2002)
22. W.J. Yuan, F.J. Liu, S.J. Pang, Y.J. Song, T. Zhang, Core loss characteristics of Fe-based amorphous alloys. Intermetallics **17**, 278–280 (2009)
23. S. Dobák, J. Füzer, P. Kollár, M. Strečková, R. Bureš, M. Fáberová, A comprehensive complex permeability approach to soft magnetic bulk cores from pure or resin coated Fe and pulverized alloys at elevated temperatures. J. Alloys Compd. **695**, 1998–2007 (2017)
24. S. Flohrer, R. Schäfer, J. McCord, S. Roth, L. Schultz, F. Fiorillo, W. Günther, G. Herzer, Dynamic magnetization process of nanocrystalline tape wound cores with transverse field-induced anisotropy. Acta Mater. **54**, 4693–4698 (2006)
25. A.N. He, S.Q. Yue, A.D. Wang, C.T. Chang, X.M. Wang, Dynamic magnetic characteristics and relaxation of $Fe_{73.5}Cu_1Nb_3Si_{15.5}B_7$ nanocrystalline alloy under operating temperature and magnetizing frequency. J. Magn. Magn. Mater. **443**, 261–266 (2017)
26. H.Y. Xiao, Y.Q. Dong, A.N. He, H. Sun, A.D. Wang, H. Li, L. Liu, X.C. Liu, R.-W. Li, Magnetic softness and magnetization dynamics of FeSiBNbCu(P, Mo) nanocrystalline alloys with good high-frequency characterization. J. Magn. Magn. Mater. **478**, 192–197 (2019)
27. X.D. Fan, M.F. Jiang, W.M. Yang, B.L. Shen, Synthesis of novel FeSiBPCCu alloys with high amorphous forming ability and good soft magnetic properties. J. Non-Cryst. Solids **503–504**, 36–43 (2019)
28. S. Kim, Y.J. Kim, Y.K. Kim, H. Choi-Yim, Annealing effect on the magnetic properties of cobalt-based amorphous alloys. Curr. Appl. Phys. **17**, 548–551 (2017)
29. A.D. Wang, C.L. Zhao, A.N. He, H. Men, C.T. Chang, X.M. Wang, Composition design of high Bs Fe-based amorphous alloys with good amorphous-forming ability. J. Alloys Compd. **656**, 729–734 (2016)
30. A. Göktaş, A. Tumbul, F. Aslan, Grain size-induced structural, magnetic and magnetoresistance properties of $Nd_{0.67}Ca_{0.33}MnO_3$ nanocrystalline thin films. J. Sol Gel Sci. Technol. **78**, 262–269 (2016)
31. A. Göktaş, F. Aslan, İ.H. Mutlu, Annealing effect on the characteristics of $La_{0.67}Sr_{0.33}MnO_3$ polycrystalline thin films produced by the sol–gel dip-coating process. J. Mater. Sci. Mater. Electron. **23** 605–611 (2011)
32. R. Schäfer, N. Mattern, stripe domains on amorphous ribbons. IEEE Trans. Magn. **32**, 4809–4811 (1966)
33. D. Azuma, R. Hasegawa, S. Saito, M. Takahashi, Effect of residual strain in Fe-based amorphous alloys on field induced magnetic anisotropy and domain structure. J. Appl. Phys. **113**, 17A339 (2013)

34. D. Azuma, R. Hasegawa, S. Saito, M. Takahashi, Domain structure and magnetization loss in a toroidal core based on an Fe-based amorphous alloy. J. Appl. Phys. **111**, 07A302 (2012)
35. A. Zhukov, J. Velázquez, C. Garcíaa, R. Valenzuela, B. Ponomarev, Frequency dependence of coercivity in rapidly quenched amorphous materials, Mater. Sci. Eng. A **226–228**, 753–756 (1997)
36. S. Dobák, J. Füzer, P. Kollár, Temperature evolution of broadband magnetization behavior in dual-phase soft magnetic compacted materials. Mater. Des. **114**, 383–390 (2017)
37. J. Szczyglowski, Influence of eddy currents on magnetic hysteresis loops in soft magnetic materials. J. Magn. Magn. Mater. **223**, 97–102 (2001)
38. S. Havriliak, S. Negami, A complex plane analysis of α-dispersions in some polymer systems. J. Polym. Sci. Part C Polym. Symp. **14**, 99–117 (1966)
39. F.R. Daró, A.C.C. Migliano, G.P. Zanella, A.K. Hirata, Y.C. De Polli, M.C.B. Salvadori, The effect of magnetic domain walls on the complex permeability of bulk Z-type cobalt hexaferrite along both W and Y-phases. Mater. Chem. Phys. **170**, 12–23 (2016)
40. G.L. Ferreira-Fraga, L.A. Borba, P. Pureur, Impedance and initial magnetic permeability of the Heusler compounds Pd_2MnSn and Pd_2MnSb near the Curie temperature. Phys. Rev. B **74**, 064427 (2006)